RF performances at cryogenic temperature of inductors integrated in a FDSOI technology

Quentin Berlingard, Jose Lugo-Alvarez, Lauriane Contamin, Cédric Durand, Philippe Galy, Andre Juge, Silvano de Franceschi, Maud Vinet, Tristan Meunier, Mikaël Cassé, et al.

Version of Record: https://www.sciencedirect.com/science/article/pii/S0038110122000570
Manuscript_12f014c806224fc543da4f7b296c9b45

RF performances at cryogenic temperature of inductors integrated in a FDSOI technology

Quentin Berlingard,
CEA Leti,
Université Grenoble Alpes,
F-38000, Grenoble, France,

Jose Lugo-Alvarez,
CEA Leti,
Université Grenoble Alpes,
F-38000, Grenoble, France,
jose.lugo@cea.fr

Lauriane Contamin,
CEA Leti,
Université Grenoble Alpes,
F-38000, Grenoble, France,

Cédric Durand,
STMicroelectronics,
850 rue Jean Monnet,
38920 Crolles, France

Philippe Galy,
STMicroelectronics,
850 rue Jean Monnet,
38920 Crolles, France

Andre Juge,
STMicroelectronics,
850 rue Jean Monnet,
38920 Crolles, France

Silvano De Franceschi,
CEA-IRIG,
Université Grenoble Alpes,
MINATEC, 38054 Grenoble, France

Maud Vinet,
CEA Leti,
Université Grenoble Alpes,
F-38000, Grenoble, France,

Tristan Meunier,
CNRS, Institut Néel,
Université Grenoble Alpes,
38042 Grenoble, France

Mikaël Cassé,
CEA Leti,
Université Grenoble Alpes,
F-38000, Grenoble, France,

Fred Gaillard,
CEA Leti,
Université Grenoble Alpes,
F-38000, Grenoble, France,

***Abstract* – This paper investigates the RF performances of octagonal inductors integrated in a Fully Depleted Silicon On Insulator (FD-SOI) technology at cryogenic temperature. The RF performances characterization of passive and active components is a first necessary step towards the design of RF circuits optimized for cryogenic CMOS applications. Among passive components, inductors are key to design low noise amplifier needed for instance in qubits read-out circuit. First, the experimental set-up and the experimental protocol is presented in detail. Then inductance with 0.5nH to 4 nH values are characterized in frequency from room temperature down to 4.2K and modelled by a lumped elements circuit. We used a simple RLC circuit to describe the self-resonance behaviour. A calculation is proposed for the inductance and the capacitance, whereas the resistance is extracted by DC measurements. This circuit description is improved by including coil proximity and skin effects. We observed that the quality factor is improved by a factor of two at low temperature, thanks to the metal resistivity decreases, in qualitative agreement with DC measurements. We also discussed the limits of the proposed model.**

***Keywords* – RF modelling, inductance, FDSOI, CryoCMOS, cryogenic RF measurements**

I. INTRODUCTION

There is an increasing range of applications for Radio-Frequency (RF) electronics at cryogenic temperature, such as control electronics for quantum computing or aerospace electronics [1][2]. For example, control circuits for quantum computers could be needed to operate as low as 100mK in the Super High Frequency (SHF) band. Such circuits will contain passive filters, attenuators and amplifiers, among other RF components. For these reasons, we need to assess performances of these circuits in a wide range of low to very low temperature, and develop the corresponding component models. Previous works showing RF measurements at low temperature (77K or lower) have focused on RF circuits such as Low Noise Amplifiers (LNA) [3], Voltage-Controlled Oscillators (VCO) [4] and transformers [5]. On-chip inductor is a critical passive component for RF circuits. Here, we study the performances of spiral inductors integrated in 28nm FDSOI technology from STMicroelectronics [10]. FDSOI circuits appear as a very promising choice for cryogenic applications, thanks to the high electrostatic integrity, low variability and threshold voltage control through the back gate provided by this technology [6–9]. In the following, we present RF characterization of inductors in a temperature range from 300K down to 4.2K. Then a model is proposed and discussed, using additional DC measurements.

II. EXPERIMENTAL SET-UP AND MEASURED INDUCTORS

We used a cryogenic probe station Lakeshore EMTTP4 to perform measurements between room temperature and 4.2 K using liquid helium. Temperature regulation over this entire range, is ensured by a LakeShore 340 Temperature Controller controlling a heater located on the sample holder. This set-up thus provides stable temperature over the measurement duration at each operation temperature.

Since the lowering and the control of the temperature is a crucial step in the cryogenic measurements, the temperature is monitored at four different places: under the sample holder, in the main chamber, on one DC probe arm and on the vacuum chamber extremity. These different temperature measurement points are indicated in Figure 1. When we reached 4.2K under the sample holder, the main chamber is

at 5.5K and the external chamber is at 7.0K. To ensure a good thermal conduction between the silicon chip and the sample holder, we glue it using silver paint. To avoid the heat dissipation by radiation, there are two radiation shields. All these precautions make it possible to limit the temperature difference between the sample holder and the sample [11].

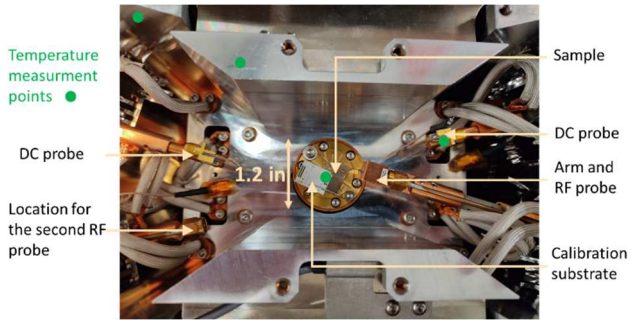

Figure 1. Prober main chamber interior for cryogenic temperature measurements. The prober used is a Lakeshore EMTTP4.

Figure 1 presents the samples and the calibration substrate on the sample holder. 300mm wafers are cleaved into smaller samples before measurement. A 1-port SOL (Short, Open, Load) calibration is realized at each temperature on a CS-5 Impedance Standard Substrate (ISS) also glued on the sample holder for an accurate and repeatable S-parameters measurement [12]. We have additionally used on-wafer open and short structures close to inductors, to de-embed the access parasitic (pads and interconnect) from the raw measurements. We performed 1-port S-parameters measurement from 500 MHz to 20 GHz using a PNA-X Keysight N5245A. The measured S_{11} parameter is then transformed into Z_{11} impedance.

The probe are lift up during the cooling (for both DC and RF measurement). Therefore, the contact resistance between the probes and RF pads can be different between each probing. The contact resistance can also slightly change because the pads are gradually degrade after a certain number of probing.

Inductors are fabricated using the last two levels of metal (top copper metal and alucap) available in the Back-end-of-Line (BEOL) of the 28nm-FDSOI technology, comprising a total of 11 levels of metal. The top copper metal is 880 nm thick and the alucap is 2155 nm thick. We have measured 18 octagonal spiral inductors with different numbers of turns n, metal track widths w and inner diameters d_{in} (Table 1). The geometry of all the inductors is illustrated in Figure 2. Note that in this 1-port test structure configuration, the inductor output is short-circuited to the ground.

Number of turn n	2	3
Inner diameter d_{in}	From 79.2 µm to 396 µm	From 158 µm to 396 µm
Metal track width w	From 13.95 µm to 23 µm	13.95 µm
Total number of n-turn inductors measured	14	4

Table 1. Parameters of the measured inductors. Each inductor have different dimensions in the range indicated.

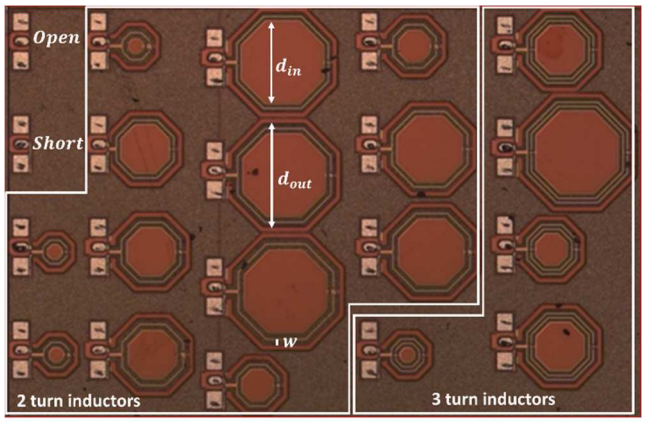

Figure 2. Octagonal FDSOI inductors measured with two or three turns and on-wafer open and short structures.

III. RESULTS AND DISCUSSION

a. *Measurements results*

All inductors of this study have a similar RF response, as well as similar temperature dependence. Figure 3 shows the inductance value, defined as $L = \frac{Im(Z11)}{\omega}$ where $\omega=2\pi f$, as a function of the frequency f, for different temperatures ranging from 300 K down to 4.2K, and the corresponding quality factor, $Q = \frac{|Im(Z_{11})|}{Re(Z_{11})}$, at 300K, 77K and 4.2K.

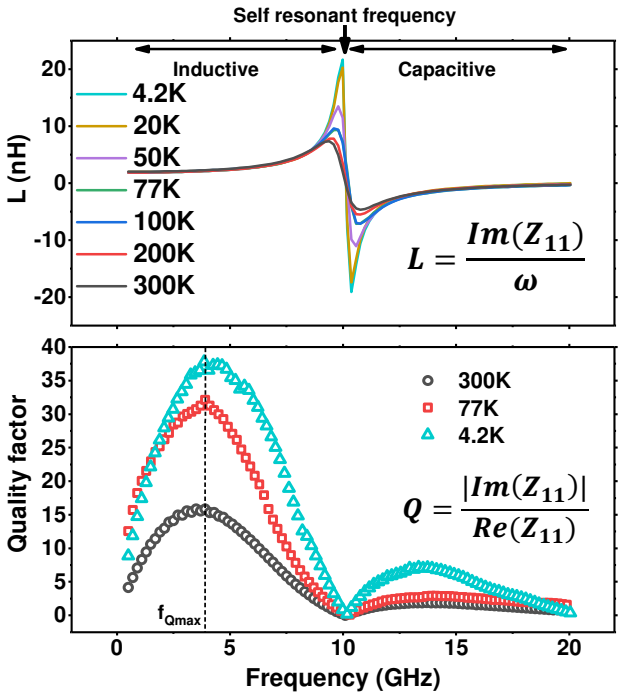

Figure 3. (Top) Inductance L measured vs frequency, and (Bottom) quality factor Q vs frequency, for different temperatures from 300K down to 4.2K. (here d_{in}=237.6 µm, w=13.95 µm and n=2).

As expected, the response is inductive at low frequency and then becomes capacitive at high frequency after the Self Resonant Frequency (SRF), here around 10GHz [13]. The

extrema values of the inductance L at low and at high frequency remains the same regardless of the temperature within our measurement accuracy, for all our measured inductors (Figure 6). Slight variations of L at low and high frequencies can be seen. They are due to measurement uncertainty such has the probing and reprobing effect and pads degradation. The main difference appears around the self-resonant frequency (see Figure 4b). Resonance occurs at the same frequency whatever the temperature, but the inductance value around this frequency increases (in absolute value,) when the temperature decreases. Moreover, the maximum of the inductance value is reached at higher frequency when the temperature decreases.

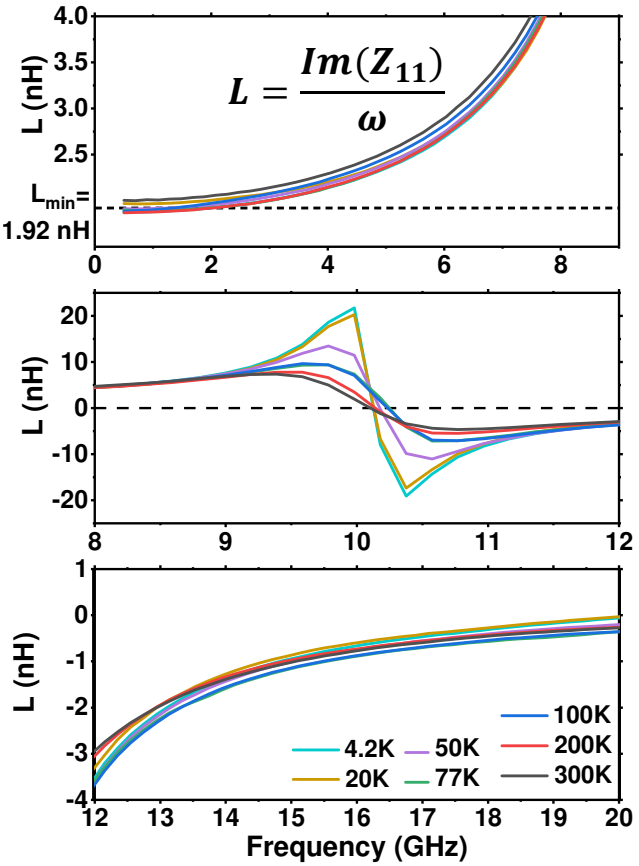

Figure 4. Zoom on the inductance L vs *f* curve shown in Figure 3 for different frequency ranges: (a) low frequenncy, (b) around self-resonance, and (c) at "high" frequency well above resonance.

The frequency at which the quality factor is maximum defines the frequency where the inductor is the most efficient The maximum of Q for a two-turn inductor with d_{in} = 237.6 µm, w = 13.95 µm is found at $f_{Q_{max}}$= 3.9 GHz regardless of the temperature (Figure 3). We observed that this maximum increases from 15 at 300K to roughly 38 at 4K as it can be seen in Figure 5. Similar increase of the quality factor maximum is observed for all the inductors studied here but the magnitude of this increase differs. This difference is discussed further in section IV.

In the following, we propose and discuss models to describe DC and frequency behaviour of our spiral inductors at low temperature.

a. Low frequency model

The measured value of the inductance at low frequency *f*=500MHz, L_{LF}, for all our two-turn inductors is presented in Figure 6 for temperature from 300 K down to 4.2K. We observed that the low frequency inductance varies linearly with d_{in}, and does not depend on temperature in this T range.

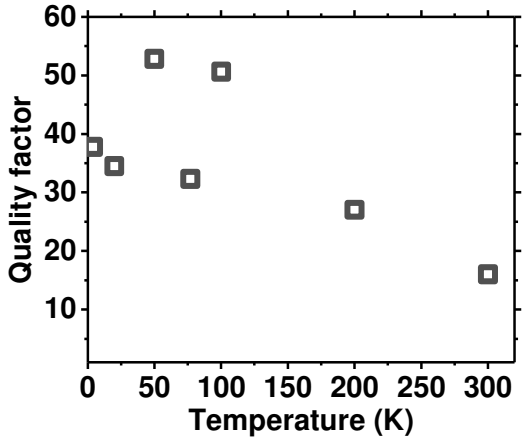

Figure 5. Maximum of quality factor Q (measured at constant f_{Qmax}) as a function of the temperature (here din=237.6 µm, w=13.95 µm and n=2).

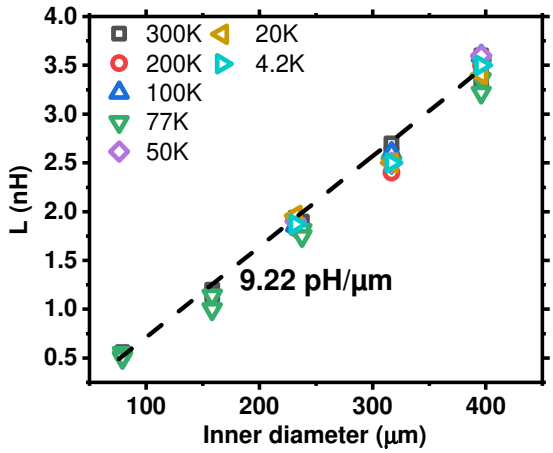

Figure 6. Inductance L_{LF} measured for 14 two-turn inductors at low frequency (500MHz), as a function of the inner diameter d_{in}, and for different temperatures.The low frequency inductance varies linearly with d_{in}, and is temperature independent.

The value of the inductance at low frequency can be express theoretically by the modified Wheeler formula [14]:

$$L_{DC,theo} = K_1 \mu_0 \frac{n^2 d_{avg}}{1 + K_2 \delta} \qquad (1)$$

Where $d_{avg} = 0.5\,(d_{out} + d_{in})$ is the average diameter, d_{in} and d_{out} are respectively the inner and outer diameter of the inductor (Figure 2), $\delta = \frac{d_{out} - d_{in}}{d_{out} + d_{in}}$ is the fill ratio, $\mu_0 = 4\pi \times 10^{-7}\, H.m^{-1}$ is the magnetic permeability of free space, n is the coil number of turns and K_1 and K_2 are layout dependent coefficients. For an octagonal inductor, $K_1 = 2.25$ and $K_2 = 3.55$ whatever its size, as given by theoretical calculation [14]. Using these coefficient values and the dimensions of our measured inductors, we calculated

the theoretical value $L_{DC,theo}$. We found a reasonably good agreement between the theoretical $L_{DC,theo}$ and the measured value L at low frequency, as can be seen in Figure 7, for all our measured two-turn inductors.

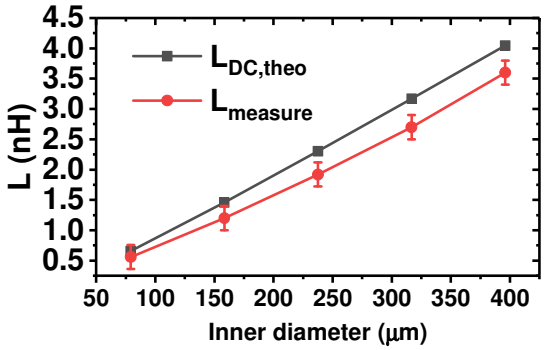

Figure 7. Comparison between the measured inductance at 500MHz and the inductance calculated using the modified Wheeler formula for two turn inductors

The error bars on the measured inductances at low frequency comes from the difference for all the measurement temperature. The small discrepancy comes from the accuracy of the measurements and the frequency used , in addition with the fact that the coefficient K_1 and K_2 are theoretical coefficient which strongly depend on the shape of the coil. K_1 and K_2 has the value for the inductors of reference [14] (which is a bit different of the measured inductors).

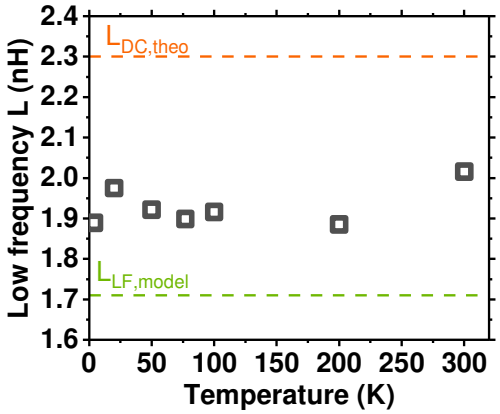

Figure 8. Inductance L measured at low frequency (f=500 MHz) as a fonction of the temperature (here d_{in}=237.6 µm, w=13.95 µm and n=2). The dash lines represents the DC theorical value of the inductance calculated in section III.b. and the low frequency value of the modeled inductance presented in section III.c.

b. Proposed RF Model

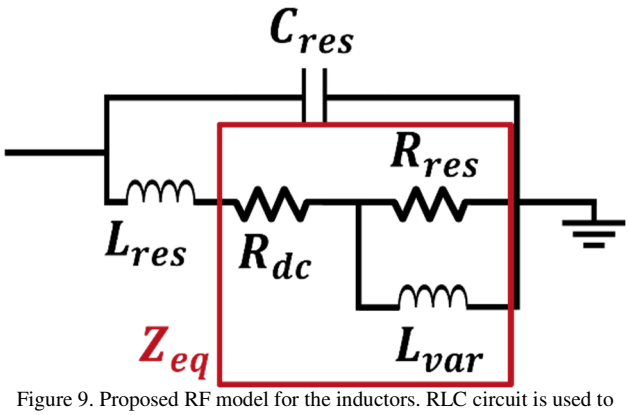

Figure 9. Proposed RF model for the inductors. RLC circuit is used to describe the self-resonance behaviour. R_{res} and L_{var} modelised the skin effect.

Figure 9 represents the RF model taken from Ref. [15]. It is composed of one main $R_{dc}L_{res}C_{res}$ loop describing the self-resonant behaviour, and one $R_{res}L_{var}$ loop for the auto induction effect, coil proximity effect and the skin effect. L_{res} and R_{dc} represent the inductance and the DC resistance introduced by the metal track. C_{res} corresponds to the parasitic capacitance in the device such as the capacitance between the different metals composing the inductor and to the pattern ground shield. The value of the parasitic capacitance has been calculated with the 2D capacitance equations of [16]. The repartition of the different parasitic capacitances and the corresponding equivalent circuit used for the calculation of C_{res} for the measured inductors are presented in Figure 10.

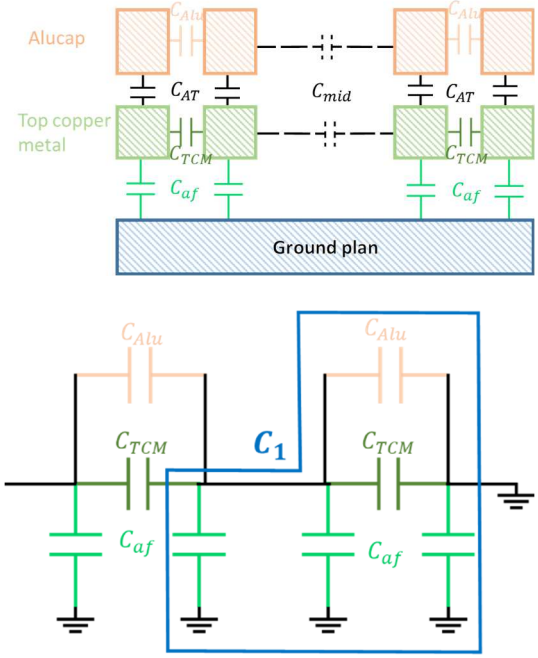

Figure 10 (Top) Schematics of the sectional view of the inductor with the parasitic capacitance repartition. (Bottom) Equivalent circuit of all the parasitic capacitances of the inductors

The capacitances C_{mid} are neglected because the inner diameter of the inductor is large enough. The capacitance C_{AT} are short-circuited by some vias. We finally obtain the following formula:

$$C_{res,theo} = C_{af} + \frac{C_1 \times (C_{TCM} + C_{Alu})}{C_1 + C_{TCM} + C_{Alu}} \qquad (2)$$

$$\text{with } C_1 = C_{TCM} + 2\,C_{af} + C_{Alu}$$

The value calculated for the studied inductors (d_{in}=237.6 µm, w=13.95 µm and n=2) is $C_{res,theo} = 0.13\ pF$.

L_{res}, C_{res} and L_{var} define the resonance frequency. R_{res} and L_{var} aim to capture the auto induction effect, the coil proximity effect and the skin effect by producing a resistance which depend on the frequency [15]. As a consequence of the skin effect, the current density inside the metal track is not uniform in all its volume when the frequency increases. The current density will be larger at the edge of the metal track. As the section available for the current becomes smaller, the resistance value of the inductor increases. Due to this skin effect, the RF resistance is thus higher than the DC resistance. The skin effect is mitigated by reducing the section of the metal track. Due to this effect, the current density decreases exponentially from the surface towards the inside.

The proximity effect is due to the inductor metal tracks proximity. The inductor track is often organised in several turns to optimize its footprint, while mitigating the resistance increase generated by skin effect. Thus, each turn will have an influence through induction on its neighbour. The current density will be modified and again, consequently the effective cross-section of the metal track becomes smaller at high frequency.

The impact of these two effect is represented by Figure 11.

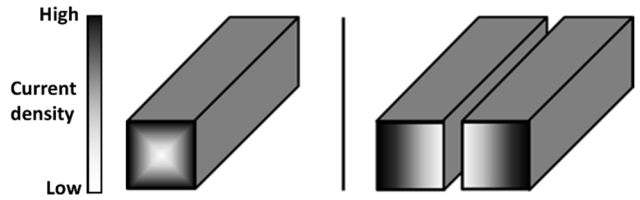

Figure 11.Schematics of the current densities repartition in inductor metal track (Left) for one track with the skin effect (Right) for two tracks closed to each other with the proximity effect [15]

This frequency-dependent resistance leads to a non-symmetrical peak of $Re(Z_{11})$ at the resonance frequency (Figure 12).

We fitted the experimental Re(Z_{11}) and Im(Z_{11}) with the model of Figure 9 using C_{res}, L_{res}, R_{res}, and L_{var} as fitting parameters, for each temperature (see values presented in Table 2). The DC resistance R_{DC} value is extracted from DC measurements presented in section III.c. The value of the capacitance C_{res} is first set to the value obtained from the previous equations. and then modified to increase the accuracy of the fit. The fit is performed on ADS® software. We found good agreement between the model and the measurements as shown in Figure 12.

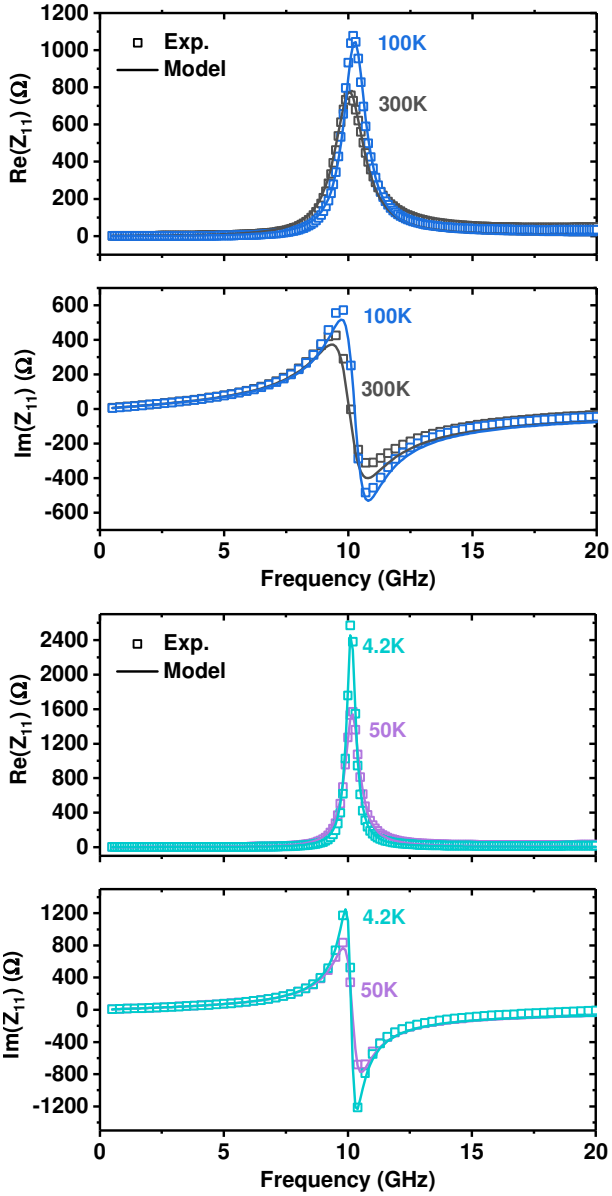

Figure 12. Inductor real and imaginary Z_{11} at 300K, 100K (Top), 50K and at 4.2K (Bottom). Measurements (dot) and model (dash). Inductor with inner diameter of 237.6 µm, a metal track width of 13.95 µm and two turns

Temperature	300 K	200 K	100 K	50 K	20 K	4.2K
C_{res}	0.145 pF	0.145 pF	0.145 pF	0.145 pF	0.145 pF	0.145 pF
L_{res}	1.25 nH	1.25 nH	1.25 nH	1.25 nH	1.25 nH	1.25 nH

R_{res}	51 Ω	58 Ω	73 Ω	111 Ω	174 Ω	185 Ω
L_{var}	0.46 nH	0.46 nH	0.46 nH	0.46 nH	0.46 nH	0.45 nH
R_{dc}	1.72 Ω	1.10 Ω	0.48 Ω	0.21 Ω	0.15 Ω	0.15 Ω

Table 2. model parameters extraction based on measurement.

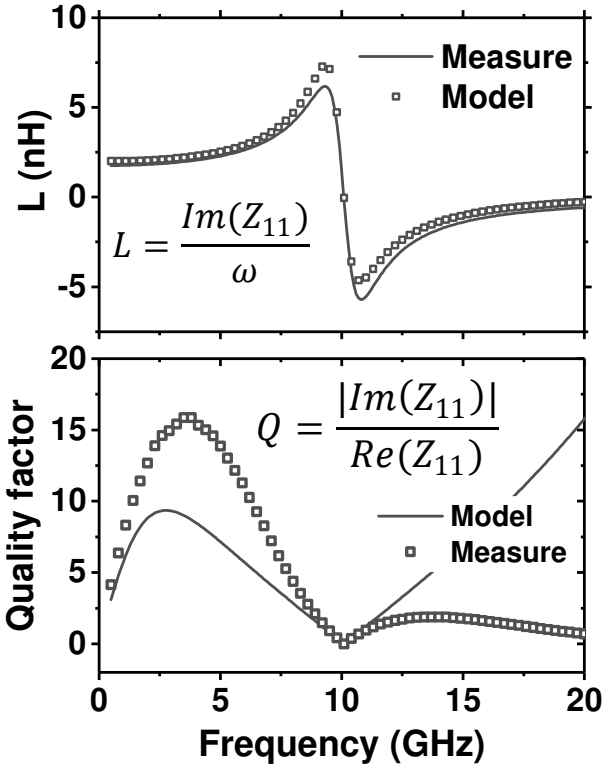

Figure 13. (Top) Inductance value and (bottom) quality factor at 300K. Measurements (dot) and model (dash).

Our model can reproduce well the measured inductance L as it is simply given by $Im(Z_{11})/\omega$ (Figure 13). On the other hand the fit of the experimental quality factor is less satisfactory, in particular the maximum value before the SRF. One possible reason may be the measurements uncertainty. Indeed, the measured inductor input resistance around Q_{max} is approximately 1 Ω. This value is below the accuracy range of the RF measurement we performed. To illustrate this limitation, Figure 14 shows the input impedance real part measured in a short circuit as a function of temperature.

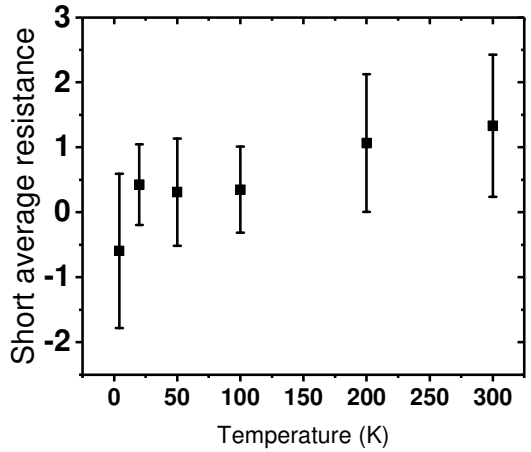

Figure 14. Real part of Z_{11} measured in a short circuit as a function of temperature. The error bars corresponds to the value at different frequency

The measured value corresponds to the mean resistance averaged in the 500 MHz–20 GHz range. The error bars correspond to the dispersion over this frequency range. Here it can be seen that with the error bars, all values overlap and the precision of measurement is approximately ±2 Ω.

IV. METAL RESISTIVITY TEMPERATURE DEPENDENCE

The capacitance C_{res} and the inductance L_{res} and L_{var} do not vary with the temperature (see Table 2), since they mainly depend on the inductor geometrical dimensions. On the other hand, R_{dc} decreases with temperature as expected and presented in [17]. This resistance reduction, due to scattering increase [17], is the main contributor of the difference between the 300 K and 4.2 K results (Figure 3 and 12). Moreover, the skin depth and the skin effect are directly dependent on the metal resistivity. According to [5], when the frequency effect can not be neglected, the inductors resistance is proportional to the square root of the material resistivity $\sqrt{\rho}$. So the modification of the temperature impact the current density repartition and the frequency dependent resistance. Therefore, R_{res} vary with temperature too.

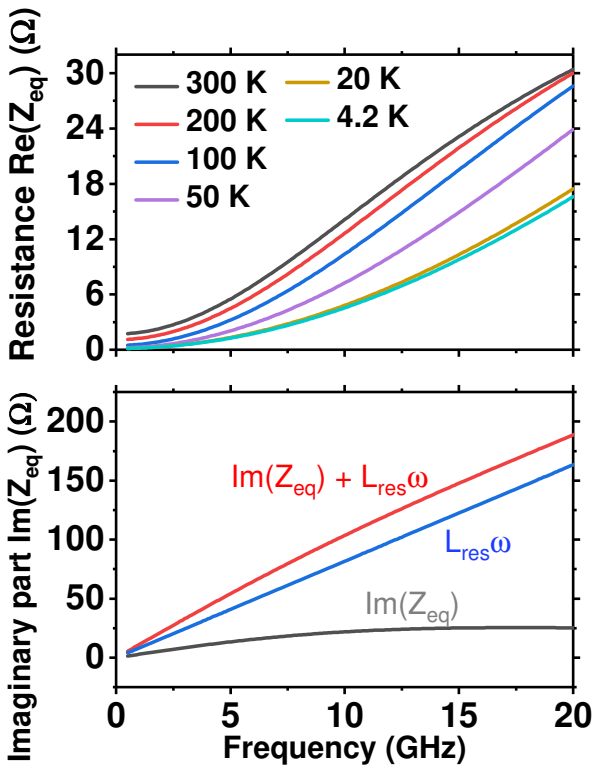

Figure 15. (Top) Effective resistance introduced by the skin effect modelled by R_{dc}, L_{var} and R_{res} as a function of frequency. (Bottom) Contribution of $L_{res}\omega$ and $Im(Z_{eq})$ to the imaginary part of Z_{11} at 300 K

Figure 15 (top) shows the variation of the effective resistance $R_{eq} = Re(Z_{eq})$ originating from R_{dc}, L_{var} and R_{res}. The formula is given in (3). When frequency increases, the resistance gets larger leading to a smaller skin depth. Besides, when temperature is lowered, $Re(Z_{eq})$ decreases since the resistivity of the metal drops. This decrease will therefore lead to an increase in R_{res} as the temperature decreases.

$$R_{eq} = Re(Z_{eq}) = R_{dc} + \frac{R_{res}L_{var}^2\omega^2}{R_{res}^2 + L_{var}^2\omega^2} \qquad (3)$$

Figure 15 (bottom) presents the contributions of $L_{res}\omega$ and $Im(Z_{eq})$ to the imaginary part of Z_{11} at ambient temperature. The formula of the imaginary part of Z_{eq} is given in (3). This figure shows that the imaginary part introduced by the inductance L_{var} and the resistance R_{res} is negligible in comparison with the imaginary part of the inductance L_{res} (which is $L_{res}\omega$). This observation is available at all measurements temperature.

$$Im(Z_{eq}) = \frac{R_{res}^2 L_{var}\omega}{R_{res}^2 + L_{var}^2\omega^2} \qquad (4)$$

To understand more precisely the variation of the resistivity of the top copper metal and alucap used in the inductor, we have performed DC measurements from 10K to 300K, as shown in Figure 16. A low DC power have been used to avoid the line self-heating, and we have performed a four-point probe measurement to de-embed contact resistance. The temperature of the device is checked with previous resistance measurements as a reference. The resistivity increases linearly with the temperature between 50K and 300K as represented by the two fits (Figure 16 (top)), which can be used for modelling. Below 50K, the decrease in resistivity saturates because scattering has been fully suppressed [18]. The observation are the same with the DC resistance of the inductor. The DC resistance extracted with this method is integrated in the model of section III.b., its value is presented in Table 2.

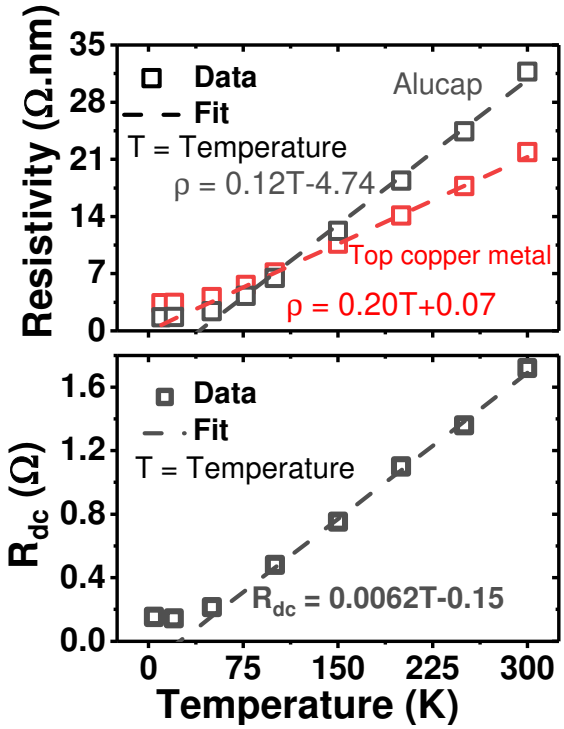

Figure 16. (top) DC resistivity of top copper metal and alucap as a function of temperature and (bottom) DC resistance of the studied inductor (stack of both metals).

V. CONCLUSION

In this work, we presented the RF characterization at cryogenic temperature of a set of inductors up to 20 GHz. A corresponding RLC model has been proposed, and validated from ambient to low temperature. Within this model, we found that the main temperature behaviour can be ascribed by the temperature dependence of the metal resistivity. In particular, it explains the improvement of the maximum quality factor with the temperature decrease. These results demonstrate the potential of the cryoelectronics, using conventional CMOS processes and materials.

VI. ACKNOWLEDGEMENTS

The authors acknowledge Spintec and especially Cécile GREZES, Laurent VILA and Aurélie KANDAZOGLOU for their help with the experimental setup. We thanks Maryline BAWEDIN from IMEP-LAHC for the proofreading of this paper. This work benefited from the facilities and expertise of the OPE)N(RA characterization platform of FMNT (FR 2542,fmnt.fr) supported by CNRS, Grenoble INP and UGA. We would like also to thank STMicroelectronics for 28FDSOI samples delivery.

VII. REFERENCES

[1] J. van Dijk et al., "Cryo-CMOS for Analog/Mixed-Signal Circuits and Systems," 2020 IEEE Custom Integrated Circuits Conference (CICC), 2020, pp. 1-8, doi: 10.1109/CICC48029.2020.9075882.

[2] E. Charbon, "Cryo-CMOS Electronics for Quantum Computing Applications," ESSCIRC 2019 - IEEE 45th Eur. Solid State Circuits Conf., pp. 1–6, 2019, doi: 10.1109/ESSCIRC.2019.8902896.

[3] M. Li et al., "Design and fabrication of cryogenic low noise amplifier in low RF band," 2007 Int. Conf. Microw. Millim. Wave Technol. ICMMT '07, pp. 8–11, 2007, doi: 10.1109/ICMMT.2007.381398.

[4] H. O. Gulec and M. B. Yelten, "A cryogenic LC VCO utilizing cryogenic models of active devices," Proc. - 2019 6th Int. Conf. Electr. Electron. Eng. ICEEE 2019, pp. 220–224, 2019, doi: 10.1109/ICEEE2019.2019.00049.

[5] B. Patra et al., "Characterization and Analysis of On-Chip Microwave Passive Components at Cryogenic Temperatures," IEEE J. Electron Devices Soc., vol. 8, no. April, pp. 448–456, 2020, doi: 10.1109/JEDS.2020.2986722.

[6] L. Nyssens et al., "28-nm FD-SOI CMOS RF Figures of Merit down to 4.2 K," IEEE J. Electron Devices Soc., vol. 8, no. December 2019, pp. 646–654, 2020, doi: 10.1109/JEDS.2020.3002201.

[7] B. C. Paz et al., "Variability Evaluation of 28nm FD-SOI Technology at Cryogenic Temperatures down to 100mK for Quantum Computing," Dig. Tech. Pap. - Symp. VLSI Technol., vol. 2020-June, pp. 7–8, 2020, doi: 10.1109/VLSITechnology18217.2020.9265034.

[8] B. Cardoso Paz et al., "Performance and Low-Frequency Noise of 22-nm FDSOI down to 4.2 K for Cryogenic Applications," IEEE Trans. Electron Devices, vol. 67, no. 11, pp. 4563–4567, 2020, doi: 10.1109/TED.2020.3021999.

[9] S. Bonen et al., "Cryogenic characterization of 22-nm FDSOI CMOS technology for quantum computing ICs," IEEE Electron Device Lett., vol. 40, no. 1, pp. 127–130, 2019, doi: 10.1109/LED.2018.2880303.

[10] N. Planes et al., "28nm FDSOI technology platform for high-speed low-voltage digital applications," Dig. Tech. Pap. - Symp. VLSI Technol., vol. 33, no. 4, pp. 133–134, 2012, doi: 10.1109/VLSIT.2012.6242497.

[11] D. R. Daughton and D. Ph, "Wafer mounting in a Lake Shore cryogenic probe station,", Application note. https://www.lakeshore.com/docs/default-source/default-document-library/wafer-mounting-in-a-lake-shore-cryogenic-probe-station.pdf

[12] J. Laskar et al., "Development of accurate on-wafer, cryogenic characterization techniques," in IEEE Transactions on Microwave Theory and Techniques, vol. 44, no. 7, pp. 1178-1183, July 1996, doi: 10.1109/22.508659.

[13] S. Bantas et al., "An inductance modeling flow seamlessly integrated in the RF IC design chain," Proc. -Design, Autom. Test Eur. DATE, vol. 3, pp. 39–43, 2004, doi: 10.1109/DATE.2004.1269196.

[14] S. S. Mohan et al. "Simple accurate expressions for planar spiral inductances," IEEE J. Solid-State Circuits, vol. 34, no. 10, pp. 1419–1420, 1999, doi: 10.1109/4.792620.

[15] Yu Cao et al., "Frequency-independent equivalent circuit model for on-chip spiral inductors," Proceedings of the IEEE 2002 Custom Integrated Circuits Conference (Cat. No.02CH37285), 2002, pp. 217-220, doi: 10.1109/CICC.2002.1012800.

[16] S. C. Wong et al., "Modeling of interconnect capacitance, delay, and crosstalk in VLSI," IEEE Trans. Semicond. Manuf., vol. 13, no. 1, pp. 108–111, 2000, doi: 10.1109/66.827350.

[17] P. Duthil, "Material properties at low temperature," CAS-CERN Accel. Sch. Supercond. Accel. - Proc., pp. 77–95, 2014, doi: 10.5170/CERN-2014-005.77.

[18] V.F. Gantmakher, "The experimental study of electron-phonon scattering in metals," Rep. Prog. Phys. 37, 317 1974.